⌘ *Author's Choice*

Structural analysis of the LDL receptor–interacting FERM domain in the E3 ubiquitin ligase IDOL reveals an obscured substrate-binding site

Luca Martinelli[1,2], Athanassios Adamopoulos[1] ⓘ, Patrik Johansson[3], Paul T. Wan[3], Jenny Gunnarsson[3], Hongwei Guo[3], Helen Boyd[3], Noam Zelcer[2,*] ⓘ, and Titia K. Sixma[1,4,*] ⓘ

From the [1]Division of Biochemistry, Netherlands Cancer Institute, Amsterdam, The Netherlands, the [2]Department of Medical Biochemistry, Amsterdam UMC, Amsterdam Cardiovascular Sciences and Gastroenterology and Metabolism, University of Amsterdam, Amsterdam, The Netherlands, the [3]IMED Biotech Unit, Discovery Sciences, AstraZeneca, Pepparedsleden 1, Mölndal, Sweden, and the [4]Oncode Institute, Utrecht, The Netherlands

Edited by George N. DeMartino

Hepatic abundance of the low-density lipoprotein receptor (LDLR) is a critical determinant of circulating plasma LDL cholesterol levels and hence development of coronary artery disease. The sterol-responsive E3 ubiquitin ligase inducible degrader of the LDLR (IDOL) specifically promotes ubiquitination and subsequent lysosomal degradation of the LDLR and thus controls cellular LDL uptake. IDOL contains an extended N-terminal FERM (4.1 protein, ezrin, radixin, and moesin) domain, responsible for substrate recognition and plasma membrane association, and a second C-terminal RING domain, responsible for the E3 ligase activity and homodimerization. As IDOL is a putative lipid-lowering drug target, we investigated the molecular details of its substrate recognition. We produced and isolated full-length IDOL protein, which displayed high autoubiquitination activity. However, *in vitro* ubiquitination of its substrate, the intracellular tail of the LDLR, was low. To investigate the structural basis for this, we determined crystal structures of the extended FERM domain of IDOL and multiple conformations of its F3ab subdomain. These reveal the archetypal F1-F2-F3 trilobed FERM domain structure but show that the F3c subdomain orientation obscures the target-binding site. To substantiate this finding, we analyzed the full-length FERM domain and a series of truncated FERM constructs by small-angle X-ray scattering (SAXS). The scattering data support a compact and globular core FERM domain with a more flexible and extended C-terminal region. This flexibility may explain the low activity *in vitro* and suggests that IDOL may require activation for recognition of the LDLR.

Hepatic low-density lipoprotein receptor (LDLR) activity is a central determinant of circulating levels of LDL cholesterol (1),

elevation of which represents a major risk factor for development of coronary artery disease. Therapeutic approaches that increase hepatic abundance of the LDLR (*e.g.* by use of statins) form the cornerstone of cholesterol-lowering strategies in hypercholesterolemic individuals (2). In view of its central role in lipoprotein metabolism, the levels, and hence activity, of the LDLR are subject to tight transcriptional regulation by the sterol-regulatory element–binding proteins (3–5). Next to transcriptional regulation, the importance of post-transcriptional control of LDLR abundance has gained recognition in recent years (6). Two central post-transcriptional pathways have been implicated in controlling LDLR abundance through regulated degradation of the receptor. The first depends on the secreted protein proprotein convertase subtilisin/kexin type 9 (PCSK9), which binds to the LDLR ectodomain and directs the normally recycling receptor toward lysosomal degradation (7–10). Targeting of this pathway through the use of anti-PCSK9 antibodies that sequester PCSK9 and prevent its interaction with the LDLR has been proven highly effective in lowering LDL cholesterol in humans (10, 11). The second pathway involves the sterol-regulated inducible degrader of the LDLR (IDOL, also known as MYLIP), which is an E3 ubiquitin ligase that promotes the ubiquitylation and subsequent lysosomal degradation of the LDLR (6, 12, 13).

Two distinct protein domains are present in IDOL: an N-terminal FERM (band 4.1/ezrin/radixin/moesin) and a C-terminal RING domain (12, 14). In contrast to secreted PCSK9, which interacts with the LDLR extracellularly, IDOL is a 45-kDa cytoplasmic protein that interacts with the intracellular tail of the LDLR via its FERM domain (12). Recognition of the intracellular tail of the LDLR is mediated by the FERM domain at the plasma membrane, and structural homology modeling facilitated the identification of a putative helix that coordinates the interaction between IDOL and a conserved motif within the intracellular tail of the LDLR (14). A similar function for the FERM domain in mediating protein-protein and membrane-protein interactions has been reported already for several other FERM domain–containing proteins (15, 16). The RING domain is needed for recruitment of the E2 ubiquitin-conjugating enzyme to IDOL, and both UBC13 and the UBE2D family of E2s have been demonstrated to work in concert with IDOL to promote sterol-dependent degradation of the LDLR (14, 17). In

addition to its role in lipid metabolism, IDOL has also been reported to trigger the ubiquitination and degradation of the very-low-density lipoprotein receptor and ApoER2 (two closely related LDLR family members), suggesting a possible role of IDOL in neuronal development and function (13, 18–20). Importantly, despite both culminating in lysosomal degradation of the LDLR, the endocytic route followed by ubiquitylated LDLR is distinct from that used by PCSK9 (21); IDOL-mediated degradation of the LDLR is clathrin- and ARH (aryl hydrocarbon receptor)-independent and requires sorting through the ESCRT (endosomal sorting complexes required for transport) system (22, 23). As such, IDOL represents an alternative and complementary post-transcriptional pathway to that governed by PCSK9 to modulate LDLR abundance.

Therapeutic targeting of IDOL, like that of PCSK9 is supported by genome-wide association studies that identified an association between variation in the *IDOL/MYLIP* locus and circulating LDL levels in humans (24). Further supporting this notion, we recently identified carriers of the first loss-of-function *IDOL* variant (25), the presence of which was associated with reduced circulating levels of LDL cholesterol. Yet targeting of IDOL may extend beyond cholesterol-lowering regimens; silencing of *Idol* expression in mice using antisense RNA protects mice from Alzheimer-like pathology (19, 26). Additionally, we recently reported that absence of *Idol* improves their glucose handling and protects *Idol*[ko] mice from dyslipidemia, obesity, and hepatosteatosis during normal aging and when challenged with a Western-type diet (27). Hence, IDOL inhibition may be broadly beneficial in metabolic-syndrome and aging-associated morbidities. However, the lack of a high-resolution structure of IDOL and a detailed description of how it interacts with the intracellular tail of the LDLR hampers development of therapeutic modalities to inhibit its activity. Here we present *in vitro* analysis of IDOL enzymatic activity showing limited LDLR peptide ubiquitination and a structural analysis of IDOL's FERM domain exploring this.

Results

Purification and characterization of recombinant full-length IDOL

Full-length IDOL consists of 445 amino acids, organized in two functional domains: an N-terminal FERM domain and a C-terminal RING domain (Fig. 1*A*) (12, 14, 28). To study IDOL ligase activity and its structure, recombinant full-length human IDOL protein was purified from insect cells.

We noticed that size-exclusion chromatography (SEC) profiles of human IDOL were characterized by multiple peaks, suggesting different oligomerization/aggregation states (Fig. S1). We then analyzed by differential scanning fluorimetry (DSF), also known as ThermoFluor, whether the IDOL purification profile was influenced by a combination of different buffer and salt conditions. In most conditions, this resulted in a profile characterized by a double transition, suggesting heterogeneity (Fig. 1*B* and Fig. S1), whereas only at low pH (pH 4–6) and intermediate NaCl concentration (500–750 mM), IDOL melting curves are characterized by a single transition (*red line* in Fig. 1*B* and Fig. S1).

We used SEC coupled with multiangle light scattering (SEC-MALS) to further analyze the effects of pH and NaCl concentration on IDOL homogeneity (Fig. S1). This revealed that IDOL runs as a dimer or larger oligomers, with peak widths that suggest polydispersity. Among the different conditions tested, its monodispersity is optimal in a buffer containing 20 mM MES, pH 6, and 500 mM NaCl. Because monodispersity can promote crystallization (29), we decided to change the IDOL purification protocol by replacing Tris buffer, pH 8, with MES buffer, pH 6, for all the purification steps and using 20 mM MES, pH 6, 500 mM NaCl, 1 mM TCEP as storage buffer.

In vitro IDOL E3 ligase activity

Using these optimized conditions for purification, we tested the ability of IDOL to promote polyubiquitin chain formation *in vitro*. Similar to what has been reported for the IDOL RING domain alone (14, 17), full-length IDOL promotes robust autoubiquitination *in vitro*. Although both E2s tested supported IDOL-mediated ubiquitination, activity is more pronounced for UBCH5C (UBE2D3) (Fig. 1*C*).

We next evaluated the activity of full-length IDOL protein against its substrate, the LDLR, using a fluorescently labeled LDLR peptide containing the IDOL recognition and ubiquitination sites (LDLR residues 811–835). We observed IDOL-dependent ubiquitin modification of the LDLR peptide, and this activity was not present on a random lysine-containing peptide or with an alternative E3 ligase, RNF168 (Fig. 1*D*). In contrast to efficient IDOL-stimulated ubiquitination of the LDLR in mammalian cells (12, 14, 17), the reaction did not seem very efficient, suggesting that IDOL is not fully active in modifying this peptide substrate or that a cell-specific activation signal is missing (Fig. 1*D*). Additionally, despite extensive attempts, no significant binding interaction could be measured with a variety of LDLR-derived peptides in fluorescence polarization or surface plasmon resonance experiments (data not shown), further supporting the notion that additional interactions, conformational changes, or post-translational modifications may be required for efficient ubiquitination.

FERM domain crystal structures

To investigate the mechanism underlying the IDOL-LDLR interaction, we therefore proceeded with structural studies. Unfortunately, neither the original purified full-length IDOL nor the protein purified under the optimized buffer conditions crystallized to allow structural determination of the full-length IDOL protein. Therefore, we purified a series of IDOL FERM domain truncations for crystallization (Fig. 1*A*). The constructs were eluted as symmetric peaks from SEC columns in purification and showed well-defined melting transitions, indicating well-folded proteins (Fig. S3). We obtained diffracting crystals for two different constructs: IDOL FERM domain, which spans residues 1–344 (FERM[344]), and the third lobe of the FERM domain, F3ab (residues 183–283).

The F3ab subdomain crystallized in space group $P2_12_12_1$, with cell dimensions a = 56.37 Å, b = 69.54 Å, c = 74.32 Å, $\alpha = \beta = \gamma = 90°$, with three subunits in the asymmetric unit and a solvent content of 43%. We collected a single crystal data set,

ASBMB

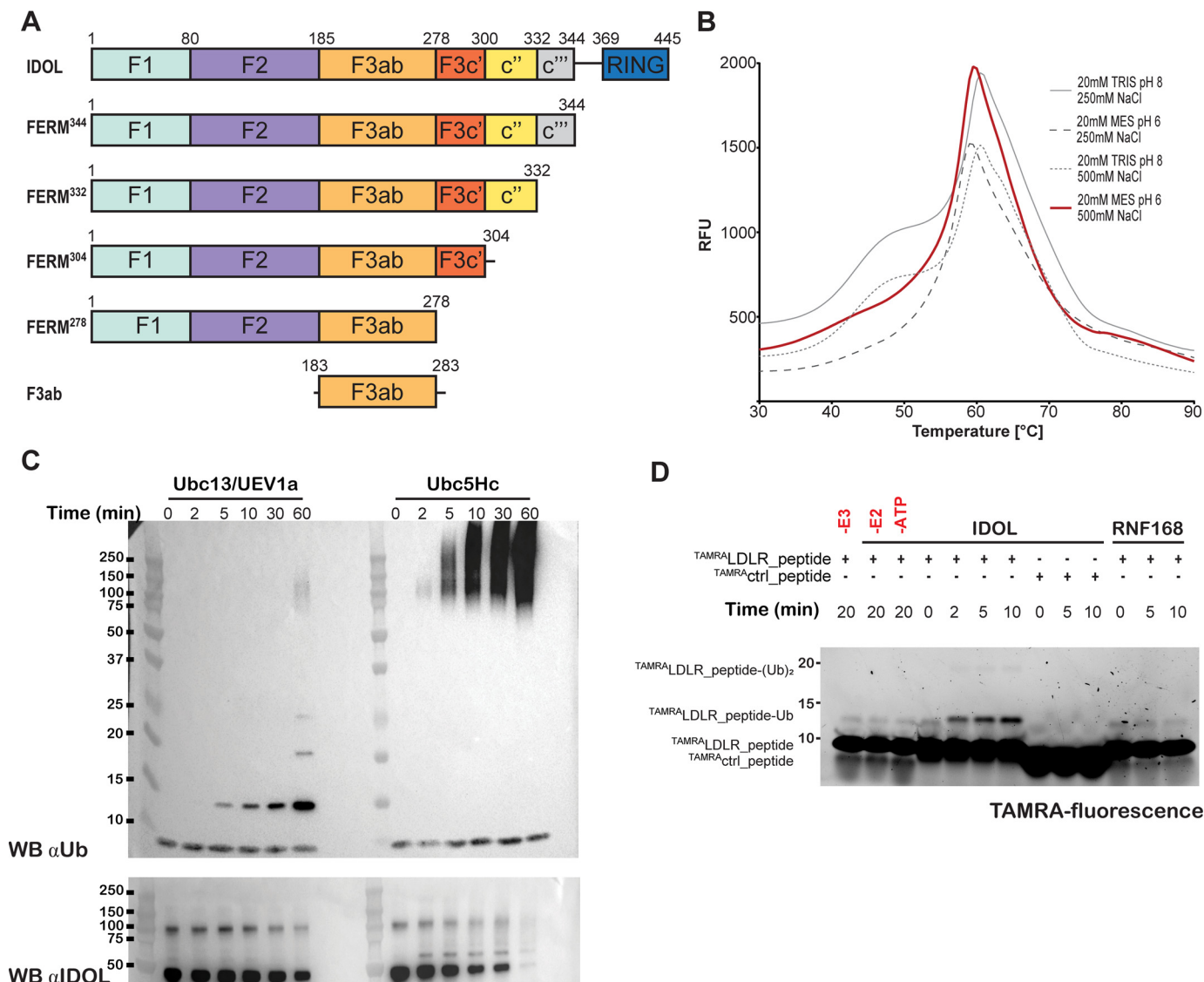*J. Biol. Chem.* (2020) 295(39) 13570–13583   **13571**

Figure 1. Characterization full-length IDOL. *A, schematic view* of the IDOL constructs used in this study. *Numbers* indicate amino acid positions. Subdomain boundaries are indicated. *B,* melting curves reflecting temperature-dependent IDOL conformational stability for full-length IDOL under different conditions. Results are shown in relative fluorescence units (*RFU*). All buffers contained 1 mM TCEP. *C, in vitro* autoubiquitination (*top*) and ubiquitin polychain formation (*bottom*) IDOL activity assay. IDOL autoubiquitination was detected by immunoblotting for IDOL, whereas ubiquitin polychain formation was detected by immunoblotting (*WB*) for ubiquitin. *D, in vitro* IDOL-dependent LDLR_peptide ubiquitination. TAMRA fluorescence signals were acquired by a ChemiDoc XRS+ imaging system (Bio-Rad).

which diffracted to 2.35 Å resolution and solved F3ab crystal structure by molecular replacement using the equivalent region from DAL-1 (PDB ID: 2HE7) as a search model. Alternate model building in *Coot* (30) and refinement in BUSTER (31) resulted in a structure with R/R_{free} of 25.4/28.4 and overall good statistics (Table 1).

The FERM[344] protein crystallized in space group I4₁22, with unit-cell parameters $a = b = 159.49$ Å, $c = 76.72$ Å, $\alpha = \beta = \gamma = 90°$, with one molecule in the asymmetric unit and a solvent content of 60%. We collected a 2.5 Å data set and solved its crystal structure by molecular replacement using the primitive monoclinic crystal structure of the FERM domain of protein 4.1R (PDB ID: 3QIJ) as search model. After several cycles of alternate model building in *Coot* and structure refinement in BUSTER and Refmac (32), we achieved a structure with R/R_{free} of 22.9/26.4% and overall good statistics (see Table 1). The

301–305 loop could not be resolved in density as well as the last 12 C-terminal residues. In addition, the loops in the F2 region are less well-defined, most likely due to flexibility.

The F1, F2, and F3 regions of FERM[344] adopt the archetypical cloverleaf structure of the FERM domains (Fig. 2A). Previous sequence analysis (28) had suggested that IDOL FERM domain could contain an apparent insertion within the F3 subdomain. However, our structure shows that F3ab runs from 186 to 278 and that the region spanning residues 279–332 is clearly outside the cloverleaf region. Based on the obtained structure, we propose to redefine IDOL FERM boundaries as shown in Fig. 1A, with the extra region in FERM (which spans residues 279–344) divided into three subdomains to accentuate the extension away from the F3ab lobe: F3c′ (residues 279–300), F3c″ (residues 301–332), and F3c‴ (residues 333–344), with the latter not traceable in the electron density map (Fig. 2A).

Table 1

X-ray data collection and refinement statistics

Values for the highest-resolution shell are shown in parentheses. RMSD, root mean square deviation.

Crystal	FERM[344]	F3ab
Data collection		
Beamline	ESRF MASSIF-1	ESRF ID23-1
Wavelength (Å)	0.966	0.979
Resolution range (Å)	56–2.40	74–2.34
Space group	I4$_1$22	P2$_1$2$_1$2$_1$
Cell parameters		
a, b, c (Å)	159.49, 159.49, 76.72	56.37, 69.54, 74.32
α, β, γ (degrees)	90, 90, 90	90, 90, 90
No. of unique reflections	19,675	12,704
Completeness (%)	99.8 (97.7)	99.3 (97.2)
Redundancy	7.1 (6.7)	4.6 (4.4)
$I/\sigma(I)$	12.7 (0.2)	11.0 (0.7)
Refinement statistics		
Resolution range (Å)	50–2.5	50–2.34
R-factor/R_{free} (%)	22.9/26.4	25.4/28.4
Reflections (working/free)	17,399/841	12,627/619
Molecules per asymmetric unit	1	3
RMSD from target		
Bond lengths (Å)	0.009	0.008
Bond angles (degrees)	1.08	1.04
Ramachandran plot		
Favored (%)	94.8	94.6
Allowed (%)	5.2	5.4
Outlier (%)	0	0

The FERM[344] subdomain F1 spans residues 1–80 and adopts a ubiquitin-like fold, consisting of a five-stranded β-sheet, a short 3$_{10}$ helix, and an α helix. Strands β1 and β5 are the first and the last β strand in the F1 subdomain, respectively, but form consecutive strands in the F1 β-sheet, resulting in an overall compact F1 domain. Subdomain F2 spans residues 81–185 and is all helical. It is composed of a four-helix bundle characteristic of the acyl-CoA–binding protein fold. The last subdomain in the traditional FERM cloverleaf is subdomain F3ab, encompassing residues 186–278. This domain resembles a phosphotyrosine-binding domain, characterized by the pleckstrin homology superfold, with seven antiparallel β-strands forming two orthogonal β-sheets capped by a C-terminal α helix (α6, residues 258–276). After the α7 helix, the FERM[344] structure has a partially unstructured region from residue 301 until residue 317, followed by helix α8 (residues 318–332) (F3c″), which is the last residue traceable in the electron density map.

The F3ab conformation is well-conserved between the FERM[344] and the three copies in the asymmetric unit of the F3ab crystal structure. There is a conformational difference in two β-turns (β6-β7 and β8-β9) in the FERM[344] structure due to crystal contacts, which results in a loss of β-sheet character for strand "β9" in this structure (Fig. S4). Moreover, there are clear differences in the F3c′ region, where the FERM[344] crystal structure has an α helix (α7), following the F3ab, which spans residues 279–300 and folds back onto the F3ab. This region has lost helical conformation in all three copies of the F3ab structure, and in one case (F3ab monomer B) even the previous helix α6 is partially unraveled (Fig. S4).

FERM[344] oligomerization state

The FERM[344] domain packs as a tetramer in the crystal created by crystallographic symmetry operations (Fig. S5). Its extended F3c′-F3c″ region (residues 279–332) interacts exten-sively with F1 and F3 of a symmetry-related molecule, burying a substantial surface area of 2537 Å^2 (Fig. 2B). This dimer has smaller crystallographic interfaces to another identical dimer (840 and 273 Å^2, respectively), generating a tetramer, with a central four-helical bundle formed by helix α7 (F3c′ subdomain) (Fig. S5).

Such packing and especially the large dimer interface could indicate that oligomerization is important for IDOL function. Therefore, we investigated the solution behavior of different IDOL constructs, using SEC-MALS. As shown in Fig. 2C, all the FERM variants presented in this study behave as monomers, indicating that the oligomerization is only relevant under crystallization conditions. The monomeric state of FERM[344] was also confirmed by small-angle X-ray scattering (SAXS) analysis (see below) (Table 2 and Fig. 2 (D and E)).

Comparison with other FERM domains

Having obtained the IDOL FERM domain structure, we proceeded to compare it with other FERM domains in the PDB.

First, we analyzed the surface charge properties of the IDOL FERM domain (Fig. 3A). Some FERM domains, such as radixin, have an inositol trisphosphate (IP$_3$)-binding site between the F1 and F3ab subdomains. Analysis of the surface properties of the IDOL FERM domain shows that the general positive character of this surface is somewhat conserved (Fig. 3B), but not all coordinating residues are. There are three lysines (Lys^{60}, Lys^{63}, and Lys^{278}) involved in the IP$_3$ binding in radixin (PDB ID: 1GC6) (36), whereas in IDOL, those residues are replaced with two arginines (Arg^{59} and Arg^{61}) and one serine (Ser^{262}), respectively, with a very different arrangement.

Using SSM (37), we performed an overall structural alignment to FERM domain structures where the full cloverleaf structure was available (Fig. 4A). Superposition of 27 structures shows that the characteristic cloverleaf structure is well-conserved in FERM[344] and that a helix similar to the F3c′ region is also observed in human moesin (PDB ID: 1E5W) (38), mouse merlin (PDB ID: 1ISN) (39), human merlin (PDB ID: 6CDS) (40), and mouse radixin (PDB ID: 1J19 and 2EMS) (41, 42). Small variations in relative positioning and orientation of the F1, F2, and F3ab domain were visible, but we observed similar variations for these subdomains between data sets from different FERM[344] crystals. A major difference in other FERM domains is the position of the F3c′ region. This is differently oriented in the IDOL FERM domain (Fig. 4B), and we could not identify an equivalent of the F3c″ subdomain in other FERM-containing proteins.

Conformation of IDOL FERM in solution

We wondered whether this unusual conformation of F3c relative to the FERM domain is relevant in solution. We used SAXS to characterize a series of FERM domain variants (see Fig. 1A) to assess the orientation of F3c′ and the extended conformation of F3c″ separately.

After checking that the scattering profiles of the FERM variants did not show any sign of possible aggregation, we performed Guinier fitting on the SAXS data to estimate the radius of gyration (R_g) (Table 2). Next, we generated dimensionless (normalized) Kratky plots (43) to assess the degree of

≋ASBMB

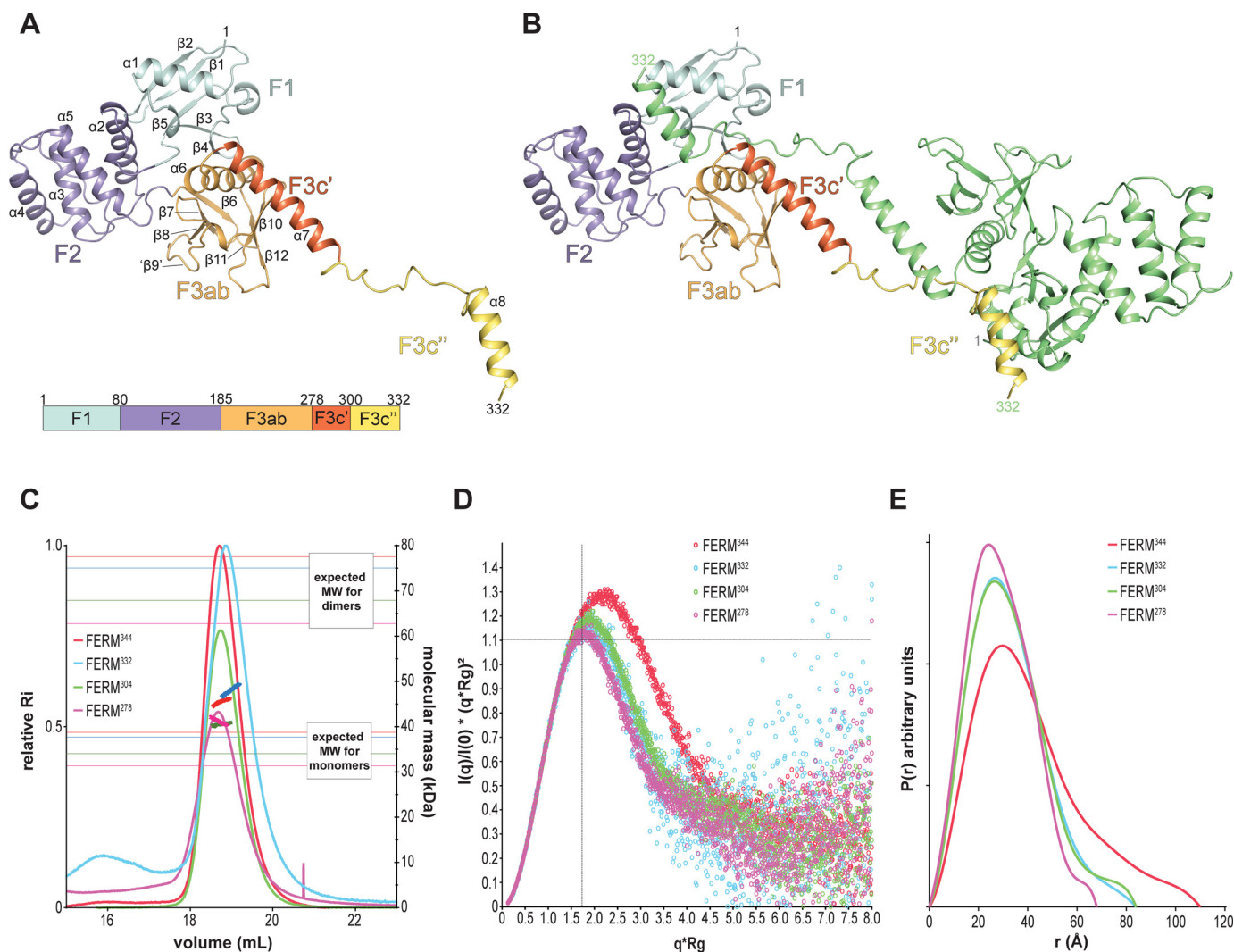*J. Biol. Chem.* (2020) 295(39) 13570–13583 **13573**

Figure 2. Crystal structure of FERM[344]. *A, cartoon representation* of the FERM[344] crystal structure. The *color scheme* is as in Fig. 1A. The N- and C-terminal residues and subdomain boundaries are indicated. Strand "β9" has lost its secondary structure propensity in FERM[344], whereas its structure is maintained in F3ab structure (see also Fig. S4). *B,* crystal contact interface between FERM[344] and symmetry-mate subunit (*colored* in *light green,* generated by symmetry operation −*x*−1,−*y*,*z*). *C,* SEC-MALS analysis of the oligomeric states of FERM variants. Refractive index profiles for all variants are shown in *thin lines,* whereas the *thick lines* (at peak position) represent the MW distribution (g/mol) of the corresponding variant. Theoretical MW of the monomeric form for each variant is reported. *D,* SAXS shape analysis. Comparison of dimensionless Kratky plots of FERM variants. FERM[278] shows the most compact conformation with the relative Kratky plot perfectly centered at $\sqrt{3}$. FERM[304] and FERM[332] show a very similar Kratky profile, with the maxima slightly shifted but still quite compact. FERM[344] shows the less compact conformation among the variants. R_g values calculated by the Guinier approximation for all the samples are listed in Table 2. *E,* SAXS pair-distribution function *P(r)* of FERM variants. FERM[278] is characterized by a unimodal distribution, indicative of a globular conformation. FERM[304] and FERM[332] have a similar D_{max}, which indicates that, despite the flexibility of F3c" domain in solution, it folds back onto the same molecule at its C terminus and that a subpopulation of extended conformations exists in solution. D_{max} and R_g values obtained from the analysis of the *P(r)* function are listed in Table 2.

compactness of the FERM truncations in solution. The dimensionless Kratky plots for all the FERM variants have a characteristic bell shape, indicative of folded and compact structures (Fig. 2D). However, only the FERM[278] variant has its peak centered closed to $\sqrt{3}$, indicative of a particularly compact structure, whereas all the other constructs have their maxima shifted to higher values of $q \times R_g$ (around 1.85 for FERM[304] and FERM[332] and around 2.25 for FERM[344]), suggesting properly folded but more elongated conformations (Table 2).

To gain more insight into the shape and the size of these FERM variants, we analyzed the pair distribution function, *P(r)*, a weighted histogram of all possible pair distances between pairs of atoms within a particle (Fig. 2E). By extrapolating the *r* values at which *P(r)* goes to zero, this analysis estimates the

maximum dimension (D_{max}) of the biomolecule in solution. FERM[304], FERM[332], and FERM[344] *P(r)* functions have a similar profile, with a noticeable tail, short for FERM[304] and FERM[332] and somewhat longer for FERM[344]. This suggests that the F3c'-F3c"-F3c''' region extends away from the body of the FERM F1-F2-F3ab and is characterized by a certain degree of flexibility. D_{max} values derived from the *P(r)* function for FERM[278] (68 Å) and FERM[304] (84 Å) are in very good agreement with their maximum dimensions calculated from the FERM[344] crystal structure, suggesting that the F3c' helix closely interacts with the F1-F2-F3ab core also in solution. The D_{max} for FERM[332] (84 Å) is not larger than that of FERM[304], indicating that in solution, the F3c" domain folds back onto the F1-F2-F3ab globular core instead of adopting the extended conformation seen in

Table 2
SAXS-derived structural parameters and fitting statistics

	SAXS experimental scattering data			
	FERM[278]	FERM[304]	FERM[332]	FERM[344]
SAXS-derived parameters				
Guinier				
R_g (Å)	22.32	25.17	24.95	32.27
$P(r)$ function				
R_g (Å)	22.32 ± 0.04	25.17 ± 0.04	24.96 ± 0.09	32.30 ± 0.06
D_{max} (Å)	68	84	84	110
MW estimation				
Q_P (kDa)[a]	26.2	35.4	33.4	54.3
MoW (kDa)[a]	32.0	39.2	38.9	59.9
V_c (kDa)[a]	29.2	34.9	34.6	50.9
Size and shape (kDa)[a]	30.3	37.9	34.6	60.2
Bayesian inference (kDa)[a]	28.9	36.9	34.6	55.6
MW based on composition				
Calculated MW (kDa)[b]	31.2	34.1	37.5	38.8
Calculated scattering data				
With CRYSOL				
FERM[278]	1.09	4.14	1.23	36.13
FERM[304]	0.97	2.83	1.11	22.92
FERM[332]	5.95	3.02	1.38	5.89
With SREFLEX				
FERM[304]		1.02	1.01	5.84
FERM[332]			1.05	1.58

[a]Derived from five independent methods (33), as implemented in PRIMUS (34). Q_p, Porod invariant; MoW, molecular weight; V_c, volume of correlation.
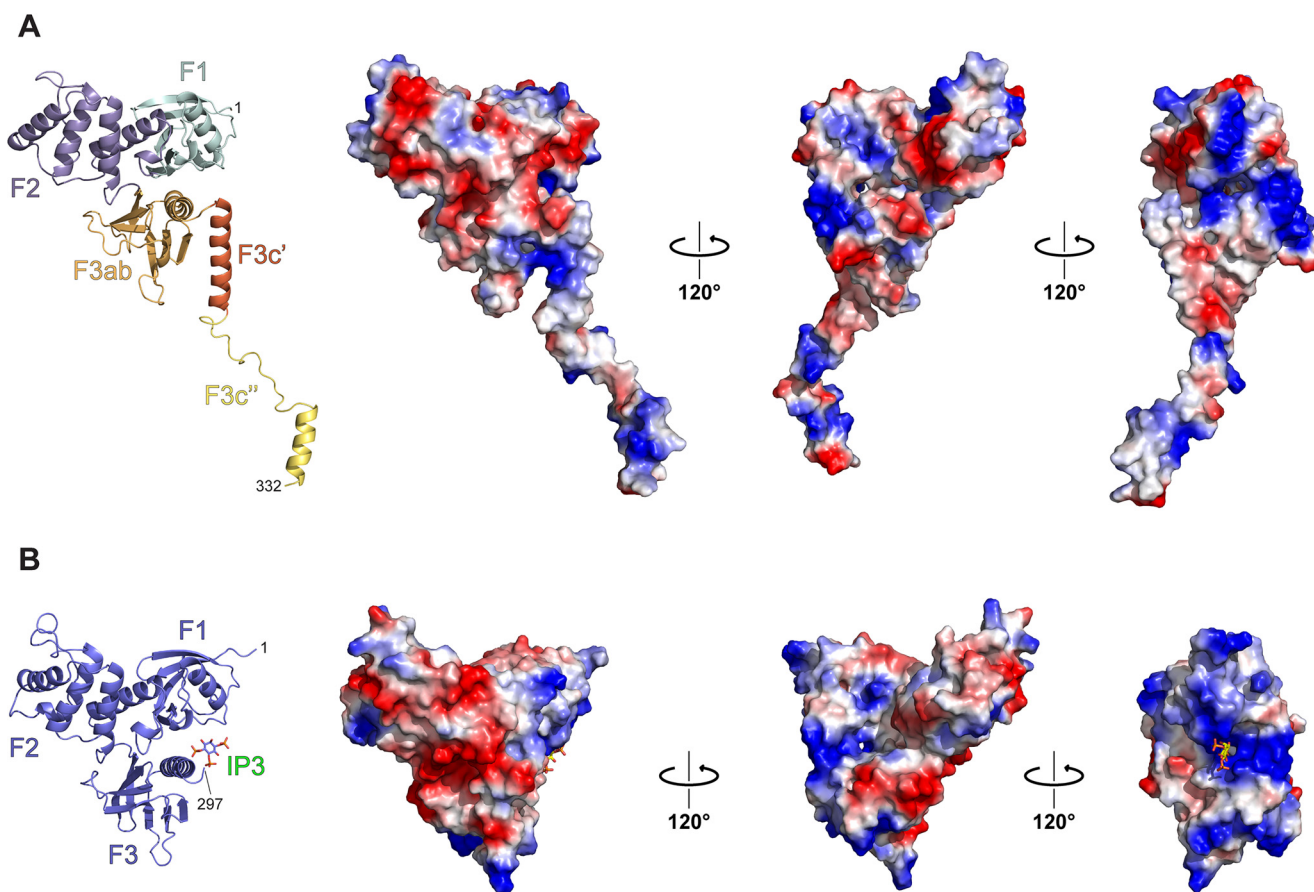[b]Calculated from primary sequence of individual truncations with the ProtParam server (RRID:SCR_018087) (35).

Figure 3. Surface charge distribution of FERM[344]. Shown is a comparison of electrostatic surface potentials of FERM[344] (*A*) and human radixin (PDB ID: 1GC6) (*B*). The electrostatic surface potentials are represented *over* the *protein surface* in *blue* and *red shades* for positively and negatively charged residues, respectively. Although positive charges are somewhat conserved around the radixin IP₃-binding site (represented in a *stick model*), the three interacting lysine residues are not conserved in IDOL.
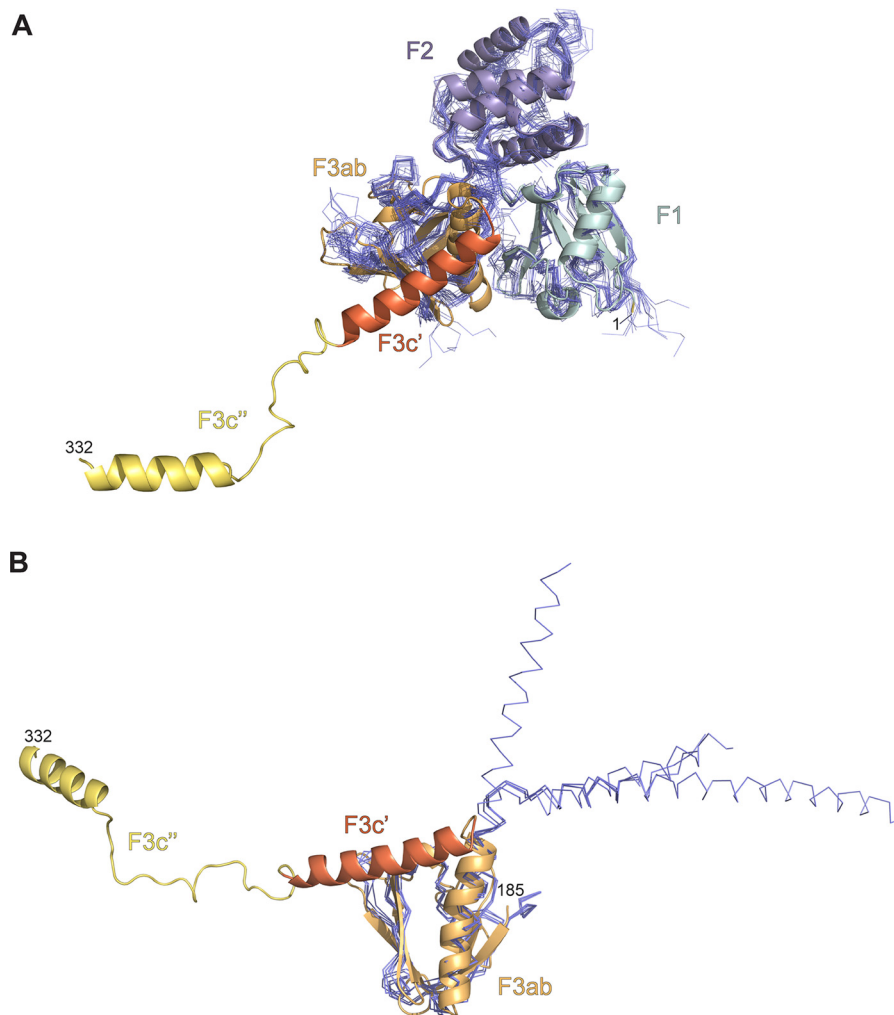
Figure 4. FERM[344] subdomain structural comparisons. *A*, overall structural comparison of FERM[344] against other FERM members. *B*, F3c' differences in other FERM domain proteins.

FERM[344] crystal structure. The extended D_{max} for FERM[344] (110 Å) shows that the last 12 C-terminal residues are highly flexible. We compared the SAXS data with calculated scattering profiles, computed from our crystal structure of the FERM domain, including only the relevant residues of FERM[278], FERM[304], and FERM[332]. The calculated data are in good agreement with the corresponding experimental scattering data, with FERM[304] having the worst fit ($\chi^2 = 2.83$; see Table 2). Interestingly, experimental scattering data collected for FERM[344] does not fit with the theoretical scattering profiles calculated with CRYSOL for either FERM[278]-, FERM[304]-, or FERM[332]-derived structures (see Table 2). However, if we allow flexibility and conformational changes of subdomains F3c' and F3c" with SREFLEX, the obtained FERM[304] and FERM[332] "flexible" models better resemble the experimental scattering data (see Table 2), supporting an intrinsic flexibility of subdomains F3c', F3c", and F3c'''. Interestingly, this keeps the F3c' bent toward the F3ab subdomain.

In conclusion, our SAXS data confirm the observation that the F3c' helix is predominantly bent back toward the bulk of the F3ab domain, whereas the F3c" and F3c''' are most likely flexible. These data suggest that the unusual orientation of the F3c' helix observed in the crystal structure is also valid in solution.

Analysis of the LDLR peptide-binding site

FERM domains are important mediators of protein-protein and protein-membrane interactions. An important conserved region in this context is the peptide interaction site within the F3ab domain. Several structures have been determined to delineate how FERM domains interact with peptides of their cognate partners at this site. For IDOL, the interaction with the LDL receptor has been mapped to this location, with residues Tyr[265], Thr[269], and His[272] being important for E3 ligase activity on the LDL receptor in cells (14, 28). The interaction in related FERM domains consists of a main-chain peptide interaction (Fig. 5, *A and B*) (41, 42, 44–47), forming an extra β-strand in the F3ab sheet, with hydrophobic side chains giving sequence specificity. Upon superposition of the FERM domain structure, the mutants most critical for binding are indeed found to line the peptide-binding groove (14, 28).

The F3c' helix obscures the LDLR peptide-binding site

In the FERM[344] structure, the F3c' is helical and positioned over the F3ab domain, obscuring the access to the peptide binding site. If this particular position is retained in full-length
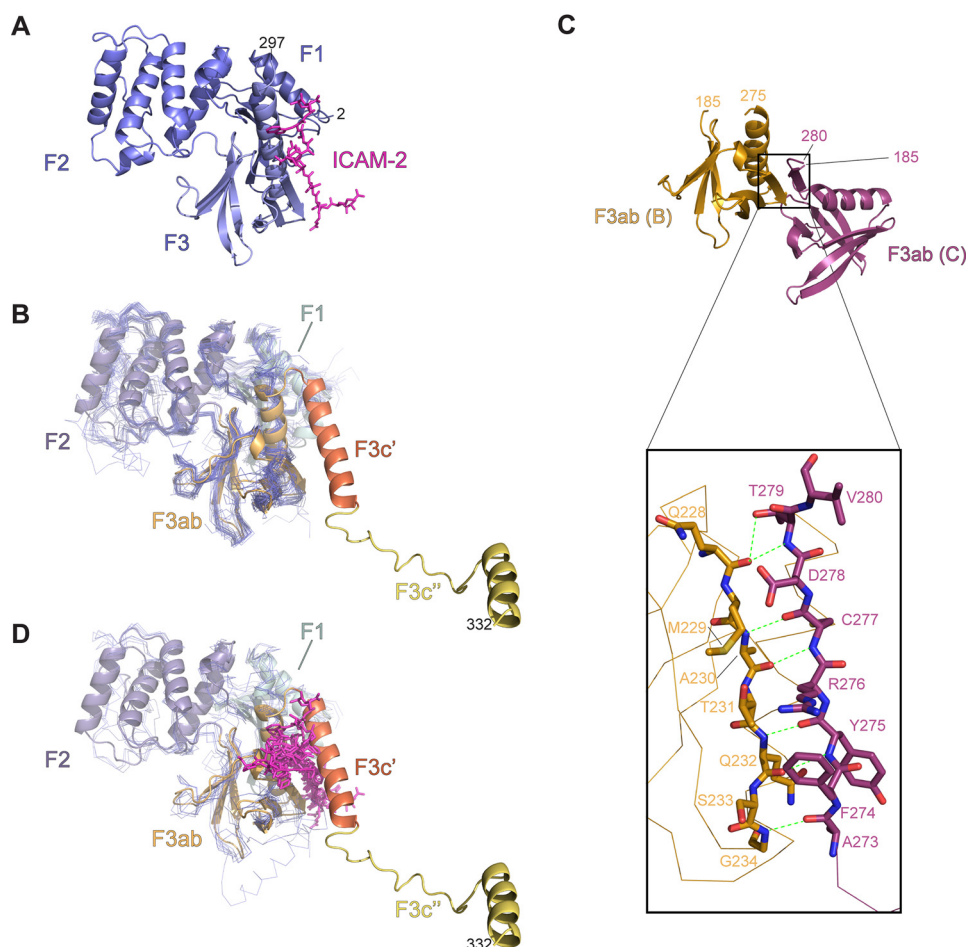
Figure 5. FERM[344] peptide-binding region. *A*, RADIXIN 1J19 FERM domain (in a *cartoon representation*, *light blue*) in complex with intercellular adhesion molecule 2 (*ICAM-2*) cytoplasmic peptide (in a *stick representation*, *magenta*). *B*, superposition of FERM domains (*blue*) on FERM[344] (*colors* according to Fig. 1A) showing how in IDOL the F3c′ subdomain closes back onto the F3ab subdomain. *C*, *ribbon representation* of F3ab crystal structure. The *color scheme* is as in Fig. 1A. Monomer B and monomer C, with respective N- and C-terminal residue boundaries are indicated. *Inset*, interaction between F3ab monomer B and the C-terminal tail of F3ab monomer C, with corresponding hydrogen bonds indicated. *D*, structural superposition of FERM[344] and FERM domain proteins complexed with their respective peptide ligands (PDB IDs used for the structural comparison: 1NTV, 1J19, 2EMS, 2ZPY, 3BIN, 4GXB, and 4TKN).

IDOL, it could prevent the interaction with the LDLR intracellular tail, suggesting a possible form of autoinhibition. Because our SAXS data suggest that this conformation is maintained in solution, it is possible that this is indeed the case. This could potentially explain the low affinity and activity observed for full-length IDOL against the LDL receptor peptide in our *in vitro* binding and ubiquitination assays. Because the expression construct used to crystallize F3ab has an incomplete F3c′, helix α7 is unfolded and helix α6 is shorter in all of the three F3ab monomer structures. In fact, in two of the three copies in the asymmetric unit, this unraveled region contacts another F3ab molecule (Fig. S4), where it takes on the role of the interacting peptide. The unraveled peptide binds in the F3ab peptide-binding site, making an interaction that closely resembles the β-β association observed in many FERM-substrate peptide complexes (Fig. 5, *C* and *D*). This confirms that the F3ab subunit is intrinsically capable of forming the peptide interaction observed in other FERM receptor interactions. However, in the FERM[344] structure, the α7 helix obscures access.

The general positive character of IDOL FERM surface may be important for membrane recognition and IDOL activity (Fig. 3). Three IDOL residues (Arg[193], Lys[199], and Arg[259]) were shown to be necessary, *in vitro*, for the recognition and interaction of IDOL with negatively charged phospholipid vesicles (28). Similarly, a R193E/K199E/R259E IDOL mutant construct showed reduced degradation of the LDLR, supporting the idea that the membrane interaction is a key component in the IDOL-LDLR interaction (28). These three residues are indeed found on the surface, in a positively charged surface patch that also includes residues Lys[50], Lys[235], and Lys[254].

It will be interesting to see whether the orieniation of the F3c′ helix is relevant in full-length IDOL. If so, this could possibly be a novel form of FERM domain autoinhibition, explaining the low ubiquitination activity of IDOL on an LDLR peptide. It is possible that the conformation of the LDLR tail in a more physiological setting (*e.g.* as part of a transmembrane protein) is critical. Alternatively, post-translational modifications of IDOL may be required for optimal recognition of the LDLR, or some form of membrane association could trigger the necessary conformational change to unmask the peptide-binding site. Ultimately, it will be interesting to see whether IDOL autoinhibition resembles the autoinhibition observed in other FERM domain proteins or if it expands the mechanisms employed for this purpose.

Crystal structures of the IDOL FERM domain

Conclusions

Here we present two crystal structures of the FERM domain of human IDOL. These structures show that although IDOL has the canonical cloverleaf structure found in FERM domains, its F3c′ adopts a conformation that may obscure substrate access to its F3ab domain. This may suggest that an additional signal is required for full activation of IDOL activity.

Experimental procedures

Cloning

Full-length human IDOL (residues 1–445) was cloned with a TEV-cleavable N-terminal His$_6$ tag into pFastbac1 for baculovirus expression. Recombinant baculovirus was generated using the Bac-to-Bac system. For the generation of FERM variants, full-length IDOL (residues 1–445) was cloned into the pET-NKI-hisSUMO2 expression vector of the NKI LIC (ligation-independent cloning) suite (48). From this pET-NKI-hisSUMO2-IDOL template, FERM variants were generated by C-terminal truncation through introduction of a premature stop codon by QuikChange site-directed mutagenesis (Agilent) immediately after IDOL residue 278 (referred to here as FERM^{278}), residue 304 (FERM^{304}), residue 332 (FERM^{332}), and residue 344 (FERM^{344}). The *E. coli* codon–optimized gene of the human F3ab subdomain (residues 183–283) with an N-terminal TEV-cleavable His$_6$ tag was purchased from GenScript and cloned into a pET28(a) vector using NcoI and XhoI restriction enzyme sites. The insect cell (full-length IDOL) and bacterial (FERM variants and F3ab subdomain) expression constructs used in this work are summarized in Fig. 1*A*.

Protein expression and purification

For full-length IDOL, *Spodoptera frugiperda* Sf21 cells cultured in Sf900II SFM medium at 27 °C were infected with baculovirus (multiplicity of infection = 2) at a cell density of 2.5–3.0 × 10^6 cells ml^{-1} and harvested after 72 h. Cell pellets were resuspended in 50 mM Tris, pH 8.0, 500 mM NaCl, 1 mM TCEP, 15 mM imidazole, Benzonase, and 1 tablet of cOmplete^{TM} protease inhibitor mixture (Sigma–Aldrich) per 50 ml of lysis buffer and lysed by sonication for 2.5 min on ice. The lysate was than centrifuged (55,000 × *g* for 1 h at 4 °C) and loaded on a 5-ml HisTrap HP column (GE Healthcare). The resin was washed with lysis buffer supplemented with buffered 25 mM imidazole, and the protein was eluted with lysis buffer supplemented with 500 mM imidazole at pH 8. The elution fractions were pooled; diluted 1:3 with 20 mM Tris, pH 8.0, 1 mM TCEP; immediately loaded on an anion-exchange column (POROS XQ, Thermo Fisher Scientific); and eluted with a linear NaCl gradient. IDOL fractions were concentrated and loaded on a size-exclusion chromatography column (Superdex S200, GE Healthcare) previously equilibrated with 20 mM Tris, pH 8, 200 mM NaCl, 1 mM TCEP. Peak fractions were concentrated to about 6 mg ml^{-1}, aliquoted, and snap-frozen in liquid nitrogen for storage.

All FERM variant plasmids were transformed into Rosetta2 (DE3) T1^R *E. coli* cells. Cells were grown in TB medium, in the presence of kanamycin and chloramphenicol, at 37 °C while shaking until the A_{600} was 1.2–1.5. Cultures were then induced

with 0.5 mM isopropyl 1-thio-β-D-galactopyranoside and allowed to grow overnight at 18 °C. Cells were harvested by centrifugation (5000 × *g* for 20 min at 4 °C) and resuspended in lysis buffer containing 50 mM Tris, pH 8, 500 mM NaCl, 1 mM TCEP, 25 mM imidazole, DNase, and one tablet of cOmplete^{TM} protease inhibitor mixture (Sigma–Aldrich) per 50 ml of lysis buffer. The purification protocol for all the FERM variants was derived from Ref. 49. Briefly, clear lysate was loaded on nickel affinity resin beads previously equilibrated with 50 mM Tris, pH 8.0, 500 mM NaCl, 1 mM TCEP, 15 mM imidazole. The resin was then washed with lysis buffer supplemented with 25 mM imidazole (pH 8), and the protein was eluted with lysis buffer supplemented with 500 mM imidazole (pH 8). SUMO tag was removed by pooling the elution fractions and incubating with SENP2 protease for 45–60 min at room temperature while dialyzing against 20 mM Tris, pH 8.0, 150 mM NaCl, 1 mM TCEP, followed by a reverse affinity chromatography step. Once cleaved, FERM variant proteins were individually buffer-exchanged to 20 mM MES, pH 6.8, 150 mM NaCl, 1 mM TCEP and immediately loaded on a cation-exchange column (POROS XS, Thermo Fisher Scientific) and eluted with a linear NaCl gradient. FERM fractions were then concentrated and loaded on a size-exclusion chromatography column (Superdex S200, GE Healthcare) previously equilibrated with 20 mM MES, pH 6.8, 300 mM NaCl, 1 mM TCEP. Peak fractions were concentrated to about 6–10 mg ml^{-1}, snap-frozen in liquid nitrogen, and aliquoted for storage.

FERM F3ab pET28(a) plasmid was transformed in BL21 (DE3) *E. coli* cells. Cells were grown in lysogeny broth medium, in presence of kanamycin, at 37 °C while shaking until the A_{600} was 0.6–0.9. Cultures were induced with 0.1 mM isopropyl 1-thio-β-D-galactopyranoside and allowed to grow overnight at 18 °C while shaking. Cells were harvested by centrifugation and resuspended in lysis buffer containing 50 mM Tris, pH 8, 300 mM NaCl, 10% glycerol, 1 mM TCEP, 25 mM imidazole supplemented with Benzonase and one tablet of cOmplete^{TM} protease inhibitor mixture and lysed by cell disruption. The lysate was than centrifuged and loaded on a 5-ml HisTrap HP column (GE Healthcare). The column was washed with lysis buffer, and the protein was eluted with lysis buffer supplemented with 350 mM imidazole at pH 8. The eluted protein was then incubated with TEV protease overnight at 4 °C while dialyzing against 50 mM Tris, pH 8, 300 mM NaCl, 10% glycerol, 1 mM TCEP, 25 mM imidazole, followed by a reverse affinity chromatography step. Cleaved F3ab protein was concentrated and loaded on a size-exclusion chromatography column (Superdex S75, GE Healthcare) previously equilibrated with 50 mM MES, pH 6.5, 500 mM NaCl, 1 mM TCEP, 10% (v/v) glycerol. Peak fractions were concentrated to about 6 mg ml^{-1}, snap-frozen in liquid nitrogen, and aliquoted for storage. In all cases, after the size-exclusion chromatographic step, the purity and homogeneity of each protein was assessed by SDS-PAGE.

Differential scanning fluorimetry for full-length IDOL

Thermal unfolding profiles of full-length IDOL (25 μl at 1 mg/ml) were recorded, in the presence of different buffer and salt compositions using DSF in a MyiQ RT-PCR system (Bio-Rad) by monitoring the fluorescent intensity of SYPRO orange

(excitation, 485 nm; emission, 575 nm) with a temperature gradient of 0.5 °C/min between 15 and 95 °C and a dwell time of 10 s/step.

Measurements of apparent T_m for FERM truncations

Temperature-dependent conformational changes were measured using nano-DSF in a Prometheus NT.48 (NanoTemper Technologies). Each FERM variant was diluted in 20 mM MES, pH 6.8, 300 mM NaCl, 1 mM TCEP to the desired concentrations. Measurements were taken over a temperature gradient of 1 °C/min between 20 and 95 °C, using an excitation power of 10%. The measured 350 nm/330 nm intensity ratios were plotted *versus* temperature. The T_m values were determined from the maximum of the first derivatives of these spectra using Prometheus NT.48 internal software.

SEC-MALS

SEC-MALS measurements were performed on an ÄKTA-purifier 100 (GE Healthcare) connected to a tri-angle detector MiniDAWN Tristar (Wyatt Technologies). For each experiment, a volume of 100 μl of 100 μM protein solution was injected into a Superdex 200 10/300 column (GE Healthcare), previously equilibrated with 20 mM MES, pH 6.8, 300 mM NaCl, and 1 mM TCEP. Molecular weights of main peaks were determined using the manufacturer's software (ASTRA) and assuming a specific refractive index increment (dn/dc) of 0.185 ml g^{-1}. Chromatographic profiles and molecular weights were plotted using Prism 7 (GraphPad).

Immunoblotting

SDS gels used were all precast 4–12, 10, or 12% BisTris gels (Thermo Fisher Scientific) run in MES or MOPS buffer (Thermo Fisher Scientific) and blotted on polyvinylidene difluoride membrane (pore size 0.45 μm; Sigma–Aldrich) with standard blotting buffer. Blocking of the Western blots was done in 5% skim milk (Merck Millipore) in PBS-Tween 20. Antibodies used for Western blotting analysis were as follows: for ubiquitin, P4D1 (horseradish peroxidase–conjugated mouse mAb from Santa Cruz Biotechnology, catalog no. sc-8017; 1:5000 dilution), MYLIP/IDOL (goat polyclonal antibody from Everest Biotech, catalog no. EB09591; 1:5000 dilution). The secondary antibody used was swine anti-goat horseradish peroxidase–conjugated from BioSource International, catalog no. ACI3404, 1:1000–2000 dilution.

In vitro ubiquitination assays

Recombinant human UBA1, UBCH5C, RNF168, and ubiquitin were purified as reported previously (50). UBC13/UEV2 was a kind gift from Dr. Ben Distel (University of Amsterdam Medical Center). *In vitro* ubiquitination reactions were carried out at 37 °C for the time indicated for each experiment, in the presence of 25 mM Tris, pH 8, 150 mM NaCl, 3 mM MgCl$_2$, 1 mM TCEP. Concentrations used were 5 mM ATP, 200 nM E1, 250 nM E2, 15 μM ubiquitin, 50 nM E3 ligase (IDOL or RNF168), and, if present, 15 μM ^{TAMRA}LDLR_peptide (residues 811–835) or a 15 μM concentration of a random ^{TAMRA}ctrl_peptide

(GPLATSTPKNNG). Reactions were stopped by the addition of SDS-PAGE loading buffer and analyzed by immunoblotting.

Crystallization

Purified FERM^{344} was concentrated using an Amicon Ultra centrifugal filter (Millipore) with a 10-kDa nominal molecular mass cutoff. Eventual dilutions were carried out using the SEC buffer (20 mM MES, pH 6.8, 300 mM NaCl, 1 mM TCEP). All the crystallization experiments were carried out using Mosquito (TTP Labtech) and 96-well two-drop MRC crystallization plates (Molecular Dimensions). Initial crystallization screenings identified few promising hits from the ComPAS suite (Qiagen) screen set up at 20 °C. After a few rounds of condition optimization, we were able to generate the crystal used in this study. Explicitly, the FERM^{344} crystal used to solve the structure was obtained with the sitting-drop vapor diffusion method at 4 °C, by mixing 100 nl of concentrated FERM^{344} protein at 5.8 mg ml^{-1} with 200 nl of reservoir solution containing 100 mM Tris, pH 8.5, 20 mM MgSO$_4$, 4% (w/v) ethylene glycol, and 12% (w/v) 2-methyl-2,4-pentanediol. Except for this condition, FERM^{344} protein also crystallized in several other similar conditions, which all contained the following components: 100 mM Tris buffer, pH 8–8.5, 10-20 mM MgSO$_4$ plus one or two alcohols at low percentage. Pyramidal-like crystals started appearing after 4–5 days and stopped growing after 2–3 weeks. Crystals were then cryoprotected via transfer into a drop of reservoir solution added with 20–25% (v/v) ethylene glycol. After incubation in the cryoprotectant solution, the crystals were looped and flash-cooled in liquid nitrogen before data collection.

The purified F3ab domain was concentrated to 5.3 mg ml^{-1} in a buffer containing 500 mM NaCl, 10% glycerol, 1 mM TCEP, and 50 mM MES, pH 6.5. Initial crystallization screening was done using the commercial Index (Hampton Research) and JCSG+ (Molecular Dimensions) screens with 150 + 150 nl vapor diffusion drops at 20 °C using a Mosquito LCP robot (TTP Labtech). Crystals from the most promising condition, containing 100 mM Hepes, pH 7.0, and 10% (w/v) PEG 6000, were flash-frozen in liquid nitrogen using 25% (v/v) glycerol as cryoprotectant and prescreened using an FR-E+ SuperBright rotating anode (Rigaku Corp.).

Data collection, structure determination, and structure analysis

X-ray diffraction data for FERM^{344} were collected at a wavelength of 0.966 Å at 100 K at the beamline MASSIF-1 ID30A-1 (ESRF, Grenoble, France) (51, 52), equipped with a PILATUS3 2M detector (DECTRIS, Baden, Switzerland). Data corresponding to the crystal structure presented in this study was collected up to 2.4 Å from a single crystal and belonged to space group I4$_1$22, with one copy per asymmetric unit. Data were indexed, integrated, and scaled with the XDS software package (53). For details of the diffraction data and the data-processing statistics see Table 1. Initial phases were obtained with Mr. BUMP (54), an automated scheme for molecular replacement (MR) in CCP4 7.0.060 (55), using 3QIJ as a search model. The initial MR solution obtained at 2.5 Å was then subjected to

several cycles of manual model building in *Coot* (30) and TLS (translation/libration/screw) restrained refinement in Refmac (32) and BUSTER (31) (Global Phasing Ltd., Cambridge UK). The structure was eventually refined against native data to 2.5 Å resolution with final R_{work} = 22.9% and final R_{free} = 26.4% (Table 1). To avoid overfitting of the structures, the PDB_REDO server (https://xtal.nki.nl/PDB_REDO/) (56) was used to determine the best relative weight for the X-ray target function and the geometry or the *B*-factor restraints for the last cycle of refinement. The quality of the final model was validated using MolProbity (57) (Table 1). The PISA (Protein Interfaces, Surfaces, and Assemblies) (58) program available in the CCP4 suite was used to compute the interface areas between the FERM[344] monomer present in the ASU and crystallographic neighbors and to predict the most stable form of multimer(s) in solution.

Full X-ray diffraction data for F3ab were collected at a wavelength of 0.979 Å at 100 K at beamline ID23-1 (ESRF, Grenoble, France), equipped with a PILATUS 6M detector (DECTRIS). Data corresponding to the F3ab crystal structure presented in this work were collected up to 2.5 Å resolution. The data were indexed and integrated with MOSFLM (59) and scaled with SCALA (60) in space group $P2_12_12_1$, with cell dimensions of 56.4, 69.5, and 74.3 Å and three copies per asymmetric unit. Initial phases were obtained by MR in PHASER (61), using the equivalent Glu[183]–Ser[283] fragment from DAL-1 (PDB ID: 2HE7) (44) as a search model. The F3ab structure was further refined by alternative cycles of model rebuilding in *Coot* and refinement in BUSTER (Global Phasing Ltd.). A final model composed of Gly[186]–Ala[283] (chain A), Tyr[185]–Tyr[275] (chain B), and Tyr[185]–Val[280] (chain C) was refined to an R/R_{free} of 25.4/28.4%. Full data collection and refinement statistics can be found in Table 1. Model-derived R_g and D_{max} for FERM[278], FERM[304], and FERM[332] were calculated with MOLEMAN (62). FERM[278] and FERM[304] models were created by truncating the model to residue 278 and residue 304, respectively. Structural images have been prepared using PyMOL (PyMOL Molecular Graphics System, version 1.7.2.1 Schrödinger, LLC, New York). SSM (37) at the European Bioinformatics Institute (RRID:SCR_004727) and the RAPIDO web server (http://webapps.embl-hamburg.de/rapido/) (63) were used to structurally align the FERM[344] PDB structure to typical members of FERM domain–containing proteins.

SAXS data collection and analysis

SAXS diffraction data were collected at 12.1 keV at beamline B21 (Diamond Light Source), equipped with a PILATUS 2M detector (DECTRIS, Switzerland). Sample-to-detector distance was 4 m. Individual samples were injected at the following concentrations: FERM[278] at 5.87 mg ml^{-1} (187 μM), FERM[304] at 7.73 mg ml^{-1} (226 μM), FERM[332] at 5.71 mg ml^{-1} (157 μM), and FERM[344] at 9.86 mg ml^{-1} (255 μM). 45 μl of each centrifuged sample were loaded onto a Superdex 200 Increase 3.2/300 column (GE Healthcare), previously equilibrated in 20 mM MES, pH 6.8, 300 mM NaCl, 1 mM TCEP. The scattering profiles from all the proteins were collected in 620 3-s frames.

SAXS data analysis was performed with both PRIMUS (34), from the ATSAS suite (64), and ScÅtter (65). Useful data range for each data set was determined with SHANUM (66). Ambiguity was measured with AMBIMETER (67), and R_g in reciprocal space was calculated with Guinier approximation (68), whereas R_g in real space was derived from pair distribution function $P(r)$. $P(r)$ functions and estimation of the D_{max} were measured with GNOM (69). CRYSOL (70) was used to calculate, based on FERM[344] and model-derived FERM[278], FERM[304], and FERM[332] structures, the theoretical scattering profile for each FERM variant and to fit it to the experimental scattering curves. Partitioning of FERM[344] crystal structure into pseudodomains based on predicted protein dynamics was done with PARCOOR (71), whereas fitting of the partitioned FERM[344] structures into the scattering data was performed with SREFLEX (71).

Data availability

Model coordinates and relative structure factors for IDOL FERM[344] and IDOL F3ab subdomain have been deposited at the Protein Data Bank in Europe (PDBe) database with accession codes 6QLY and 6QLZ, respectively. Other data will be stored in the NKI repository, available upon request from Titia Sixma (t.sixma@nki.nl).

Abbreviations—The abbreviations used are: LDLR, low-density lipoprotein receptor; ApoER2, apolipoprotein E receptor 2; DSF, differential scanning fluorimetry; FERM, band 4.1/ezrin/radixin/

moesin domain; IDOL, inducible degrader of the LDLR; LDL, low-density lipoprotein; MW, molecular weight; MYLIP, myosin regulatory light chain–interacting protein; PCSK9, proprotein convertase subtilisin/kexin type 9; PDB, Protein Data Bank; RING, really interesting new gene; SAXS, small-angle X-ray scattering; SEC, size-exclusion chromatography; SEC-MALS, size-exclusion chromatography coupled with multiangle light scattering; SSM, secondary structure matching; SUMO, small ubiquitin-like modifier; TAMRA, carboxylic acid–functionalized tetramethylrhodamine; TCEP, tris (2-carboxyethyl)phosphine; TEV, tobacco etch virus; IP$_3$, inositol trisphosphate; SUMO, small ubiquitin-like modifier; MR molecular replacement; BisTris, 2-[bis(2-hydroxyethyl)amino]-2-(hydroxymethyl)propane-1,3-diol.

References

1. Brown, M. S., and Goldstein, J. L. (1986) A receptor-mediated pathway for cholesterol homeostasis. *Science* **232,** 34–47 CrossRef Medline

2. Baigent, C., Blackwell, L., Emberson, J., Holland, L. E., Reith, C., Bhala, N., Peto, R., Barnes, E. H., Keech, A., Simes, J., and Collins, R. (2010) Efficacy and safety of more intensive lowering of LDL cholesterol: a meta-analysis of data from 170,000 participants in 26 randomised trials. *Lancet* **376,** 1670–1681 CrossRef Medline

3. Yokoyama, C., Wang, X., Briggs, M. R., Admon, A., Wu, J., Hua, X., Goldstein, J. L., and Brown, M. S. (1993) SREBP-1, a basic-helix-loop-helix-leucine zipper protein that controls transcription of the low density lipoprotein receptor gene. *Cell* **75,** 187–197 CrossRef Medline

4. Hua, X., Yokoyama, C., Wu, J., Briggs, M. R., Brown, M. S., Goldstein, J. L., and Wang, X. (1993) SREBP-2, a second basic-helix-loop-helix-leucine zipper protein that stimulates transcription by binding to a sterol regulatory element. *Proc. Natl. Acad. Sci. U. S. A.* **90,** 11603–11607 CrossRef Medline

5. Goldstein, J. L., DeBose-Boyd, R. A., and Brown, M. S. (2006) Protein sensors for membrane sterols. *Cell* **124,** 35–46 CrossRef Medline

6. Sorrentino, V., and Zelcer, N. (2012) Post-transcriptional regulation of lipoprotein receptors by the E3-ubiquitin ligase inducible degrader of the low-density lipoprotein receptor. *Curr. Opin. Lipidol.* **23,** 213–219 CrossRef Medline

7. Abifadel, M., Varret, M., Rabès, J. P., Allard, D., Ouguerram, K., Devillers, M., Cruaud, C., Benjannet, S., Wickham, L., Erlich, D., Derré, A., Villéger, L., Farnier, M., Beucler, I., Bruckert, E., *et al.* (2003) Mutations in PCSK9 cause autosomal dominant hypercholesterolemia. *Nat. Genet.* **34,** 154–156 CrossRef Medline

8. Cohen, J., Pertsemlidis, A., Kotowski, I. K., Graham, R., Garcia, C. K., and Hobbs, H. H. (2005) Low LDL cholesterol in individuals of African descent resulting from frequent nonsense mutations in PCSK9. *Nat. Genet.* **37,** 161–165 CrossRef Medline

9. Lagace, T. A., Curtis, D. E., Garuti, R., McNutt, M. C., Park, S. W., Prather, H. B., Anderson, N. N., Ho, Y. K., Hammer, R. E., and Horton, J. D. (2006) Secreted PCSK9 decreases the number of LDL receptors in hepatocytes and in livers of parabiotic mice. *J. Clin. Invest.* **116,** 2995–3005 CrossRef Medline

10. Seidah, N. G., Awan, Z., Chrétien, M., and Mbikay, M. (2014) PCSK9: a key modulator of cardiovascular health. *Circ. Res.* **114,** 1022–1036 CrossRef Medline

11. Stein, E. A., Mellis, S., Yancopoulos, G. D., Stahl, N., Logan, D., Smith, W. B., Lisbon, E., Gutierrez, M., Webb, C., Wu, R., Du, Y., Kranz, T., Gasparino, E., and Swergold, G. D. (2012) Effect of a monoclonal antibody to PCSK9 on LDL cholesterol. *N. Engl. J. Med.* **366,** 1108–1118 CrossRef

12. Zelcer, N., Hong, C., Boyadjian, R., and Tontonoz, P. (2009) LXR regulates cholesterol uptake through Idol-dependent ubiquitination of the LDL receptor. *Science* **325,** 100–104 CrossRef Medline

13. van Loon, N. M., Lindholm, D., and Zelcer, N. (2019) The E3 ubiquitin ligase inducible degrader of the LDL receptor/myosin light chain interacting protein in health and disease. *Curr. Opin. Lipidol.* **30,** 192–197 CrossRef Medline

14. Sorrentino, V., Scheer, L., Santos, A., Reits, E., Bleijlevens, B., and Zelcer, N. (2011) Distinct functional domains contribute to degradation of the low density lipoprotein receptor (LDLR) by the E3 ubiquitin ligase inducible degrader of the LDLR (IDOL). *J. Biol. Chem.* **286,** 30190–30199 CrossRef Medline

15. Yonemura, S., Hirao, M., Doi, Y., Takahashi, N., Kondo, T., Tsukita, S., and Tsukita, S. (1998) Ezrin/radixin/moesin (ERM) proteins bind to a positively charged amino acid cluster in the juxta-membrane cytoplasmic domain of CD44, CD43, and ICAM-2. *J. Cell Biol.* **140,** 885–895 CrossRef Medline

16. Mangeat, P., Roy, C., and Martin, M. (1999) ERM proteins in cell adhesion and membrane dynamics. *Trends Cell Biol.* **9,** 187–192 CrossRef Medline

17. Zhang, L., Fairall, L., Goult, B. T., Calkin, A. C., Hong, C., Millard, C. J., Tontonoz, P., and Schwabe, J. W. (2011) The IDOL-UBE2D complex mediates sterol-dependent degradation of the LDL receptor. *Genes Dev.* **25,** 1262–1274 CrossRef Medline

18. Hong, C., Duit, S., Jalonen, P., Out, R., Scheer, L., Sorrentino, V., Boyadjian, R., Rodenburg, K. W., Foley, E., Korhonen, L., Lindholm, D., Nimpf, J., van Berkel, T. J., Tontonoz, P., and Zelcer, N. (2010) The E3 ubiquitin ligase IDOL induces the degradation of the low density lipoprotein receptor family members VLDLR and ApoER2. *J. Biol. Chem.* **285,** 19720–19726 CrossRef Medline

19. Choi, J., Gao, J., Kim, J., Hong, C., Kim, J., and Tontonoz, P. (2015) The E3 ubiquitin ligase Idol controls brain LDL receptor expression, ApoE clearance, and Aβ amyloidosis. *Sci. Transl. Med.* **7,** 314ra184 CrossRef Medline

20. Gao, J., Marosi, M., Choi, J., Achiro, J. M., Kim, S., Li, S., Otis, K., Martin, K. C., Portera-Cailliau, C., and Tontonoz, P. (2017) The E3 ubiquitin ligase IDOL regulates synaptic ApoER2 levels and is important for plasticity and learning. *Elife* **6,** e29178 CrossRef Medline

21. Wang, Y., Huang, Y., Hobbs, H. H., and Cohen, J. C. (2012) Molecular characterization of proprotein convertase subtilisin/kexin type 9-mediated degradation of the LDLR. *J. Lipid Res.* **53,** 1932–1943 CrossRef Medline

22. Sorrentino, V., Nelson, J. K., Maspero, E., Marques, A. R., Scheer, L., Polo, S., and Zelcer, N. (2013) The LXR-IDOL axis defines a clathrin-, caveolae-, and dynamin-independent endocytic route for LDLR internalization and lysosomal degradation. *J. Lipid Res.* **54,** 2174–2184 CrossRef Medline

23. Scotti, E., Calamai, M., Goulbourne, C. N., Zhang, L., Hong, C., Lin, R. R., Choi, J., Pilch, P. F., Fong, L. G., Zou, P., Ting, A. Y., Pavone, F. S., Young, S. G., and Tontonoz, P. (2013) IDOL stimulates clathrin-independent endocytosis and multivesicular body-mediated lysosomal degradation of the low-density lipoprotein receptor. *Mol. Cell. Biol.* **33,** 1503–1514 CrossRef Medline

24. Teslovich, T. M., Musunuru, K., Smith, A. V., Edmondson, A. C., Stylianou, I. M., Koseki, M., Pirruccello, J. P., Ripatti, S., Chasman, D. I., Willer, C. J., Johansen, C. T., Fouchier, S. W., Isaacs, A., Peloso, G. M., Barbalic, M., *et al.* (2010) Biological, clinical and population relevance of 95 loci for blood lipids. *Nature* **466,** 707–713 CrossRef Medline

25. Sorrentino, V., Fouchier, S. W., Motazacker, M. M., Nelson, J. K., Defesche, J. C., Dallinga-Thie, G. M., Kastelein, J. J., Kees Hovingh, G., and Zelcer, N. (2013) Identification of a loss-of-function inducible degrader of the low-density lipoprotein receptor variant in individuals with low circulating low-density lipoprotein. *Eur. Heart J.* **34,** 1292–1297 CrossRef Medline

26. Van Loon, N. M., and Zelcer, N. (2016) Idolizing the clearance of amyloid-β by microglia. *Ann. Transl. Med.* **4,** 536 CrossRef Medline

27. van Loon, N. M., Ottenhoff, R., Kooijman, S., Moeton, M., Scheij, S., Roscam Abbing, R. L. P., Gijbels, M. J. J., Levels, J. H. M., Sorrentino, V., Berbée, J. F. P., Rensen, P. C. N., and Zelcer, N. (2018) Inactivation of the E3 ubiquitin ligase IDOL attenuates diet-induced obesity and metabolic dysfunction in mice. *Arterioscler. Thromb. Vasc. Biol.* **38,** 1785–1795 CrossRef Medline

28. Calkin, A. C., Goult, B. T., Zhang, L., Fairall, L., Hong, C., Schwabe, J. W., and Tontonoz, P. (2011) FERM-dependent E3 ligase recognition is a

⧘ASBMB

J. Biol. Chem. (2020) 295(39) 13570–13583 **13581**

conserved mechanism for targeted degradation of lipoprotein receptors. *Proc. Natl. Acad. Sci. U. S. A.* **108,** 20107–20112 CrossRef Medline

29. Zulauf, M., and D'Arcy, A. (1992) Light scattering of proteins as a criterion for crystallization. *J. Cryst. Growth* **122,** 102–106 CrossRef

30. Emsley, P., Lohkamp, B., Scott, W. G., and Cowtan, K. (2010) Features and development of Coot. *Acta Crystallogr. D Biol. Crystallogr.* **66,** 486–501 CrossRef Medline

31. Bricogne, G., Blanc, E., Brandl, M., Flensburg, C., Keller, P., Paciorek, W., Roversi, P., Sharff, A., Smart, O. S., Vonrhein, C., and Womack, T. O. (2017) *BUSTER*, version 2.10.3, Global Phasing Ltd., Cambridge, UK

32. Winn, M. D., Isupov, M. N., and Murshudov, G. N. (2001) Use of TLS parameters to model anisotropic displacements in macromolecular refinement. *Acta Crystallogr. D Biol. Crystallogr.* **57,** 122–133 CrossRef Medline

33. Hajizadeh, N. R., Franke, D., Jeffries, C. M., and Svergun, D. I. (2018) Consensus Bayesian assessment of protein molecular mass from solution X-ray scattering data. *Sci. Rep.* **8,** 7204 CrossRef Medline

34. Konarev, P. V., Volkov, V. V., Sokolova, A. V., Koch, M. H. J., and Svergun, D. I. (2003) PRIMUS: a Windows PC-based system for small-angle scattering data analysis. *J. Appl. Crystallogr.* **36,** 1277–1282 CrossRef

35. Gasteiger, E., Hoogland, C., Gattiker, A., Duvaud, S. e., Wilkins, M. R., Appel, R. D., and Bairoch, A. (2005) Protein identification and analysis tools on the ExPASy server. In *The Proteomics Protocols Handbook* (Walker, J. M., ed) pp. 571–607, Humana Press, Totowa, NJ

36. Hamada, K., Shimizu, T., Matsui, T., Tsukita, S., and Hakoshima, T. (2000) Structural basis of the membrane-targeting and unmasking mechanisms of the radixin FERM domain. *EMBO J.* **19,** 4449–4462 CrossRef Medline

37. Krissinel, E., and Henrick, K. (2004) Secondary-structure matching (SSM), a new tool for fast protein structure alignment in three dimensions. *Acta Crystallogr. D Biol. Crystallogr.* **60,** 2256–2268 CrossRef Medline

38. Edwards, S. D., and Keep, N. H. (2001) The 2.7 Å crystal structure of the activated FERM domain of moesin: an analysis of structural changes on activation. *Biochemistry* **40,** 7061–7068 CrossRef Medline

39. Shimizu, T., Seto, A., Maita, N., Hamada, K., Tsukita, S., Tsukita, S., and Hakoshima, T. (2002) Structural basis for neurofibromatosis type 2. Crystal structure of the merlin FERM domain. *J. Biol. Chem.* **277,** 10332–10336 CrossRef Medline

40. Chinthalapudi, K., Mandati, V., Zheng, J., Sharff, A. J., Bricogne, G., Griffin, P. R., Kissil, J., and Izard, T. (2018) Lipid binding promotes the open conformation and tumor-suppressive activity of neurofibromin 2. *Nat. Commun.* **9,** 1338 CrossRef Medline

41. Hamada, K., Shimizu, T., Yonemura, S., Tsukita, S., Tsukita, S., and Hakoshima, T. (2003) Structural basis of adhesion-molecule recognition by ERM proteins revealed by the crystal structure of the radixin-ICAM-2 complex. *EMBO J.* **22,** 502–514 CrossRef Medline

42. Takai, Y., Kitano, K., Terawaki, S., Maesaki, R., and Hakoshima, T. (2008) Structural basis of the cytoplasmic tail of adhesion molecule CD43 and its binding to ERM proteins. *J. Mol. Biol.* **381,** 634–644 CrossRef Medline

43. Rambo, R. P., and Tainer, J. A. (2011) Characterizing flexible and intrinsically unstructured biological macromolecules by SAS using the Porod-Debye law. *Biopolymers* **95,** 559–571 CrossRef Medline

44. Busam, R. D., Thorsell, A. G., Flores, A., Hammarström, M., Persson, C., Öbrink, B., and Hallberg, B. M. (2011) Structural basis of tumor suppressor in lung cancer 1 (TSLC1) binding to differentially expressed in adenocarcinoma of the lung (DAL-1/4.1B). *J. Biol. Chem.* **286,** 4511–4516 CrossRef Medline

45. Mori, T., Kitano, K., Terawaki, S., Maesaki, R., Fukami, Y., and Hakoshima, T. (2008) Structural basis for CD44 recognition by ERM proteins. *J. Biol. Chem.* **283,** 29602–29612 CrossRef Medline

46. Ghai, R., Bugarcic, A., Liu, H., Norwood, S. J., Skeldal, S., Coulson, E. J., Li, S. S., Teasdale, R. D., and Collins, B. M. (2013) Structural basis for endosomal trafficking of diverse transmembrane cargos by PX-FERM proteins. *Proc. Natl. Acad. Sci. U. S. A.* **110,** E643–E652 CrossRef Medline

47. Stiegler, A. L., Zhang, R., Liu, W., and Boggon, T. J. (2014) Structural determinants for binding of sorting nexin 17 (SNX17) to the cytoplasmic adaptor protein Krev interaction trapped 1 (KRIT1). *J. Biol. Chem.* **289,** 25362–25373 CrossRef Medline

48. Luna-Vargas, M. P., Christodoulou, E., Alfieri, A., van Dijk, W. J., Stadnik, M., Hibbert, R. G., Sahtoe, D. D., Clerici, M., Marco, V. D., Littler, D., Celie, P. H., Sixma, T. K., and Perrakis, A. (2011) Enabling high-throughput ligation-independent cloning and protein expression for the family of ubiquitin specific proteases. *J. Struct. Biol.* **175,** 113–119 CrossRef Medline

49. Mori, T., Kitano, K., Terawaki, S., Maesaki, R., and Hakoshima, T. (2007) Crystallographic characterization of the radixin FERM domain bound to the cytoplasmic tail of adhesion molecule CD44. *Acta Crystallogr. Sect. F Struct. Biol. Cryst. Commun.* **63,** 844–847 CrossRef Medline

50. Mattiroli, F., Vissers, J. H., van Dijk, W. J., Ikpa, P., Citterio, E., Vermeulen, W., Marteijn, J. A., and Sixma, T. K. (2012) RNF168 ubiquitinates K13-15 on H2A/H2AX to drive DNA damage signaling. *Cell* **150,** 1182–1195 CrossRef Medline

51. Bowler, M. W., Nurizzo, D., Barrett, R., Beteva, A., Bodin, M., Caserotto, H., Delagenière, S., Dobias, F., Flot, D., Giraud, T., Guichard, N., Guijarro, M., Lentini, M., Leonard, G. A., McSweeney, S., *et al.* (2015) MASSIF-1: a beamline dedicated to the fully automatic characterization and data collection from crystals of biological macromolecules. *J. Synchrotron Radiat.* **22,** 1540–1547 CrossRef Medline

52. Svensson, O., Malbet-Monaco, S., Popov, A., Nurizzo, D., and Bowler, M. W. (2015) Fully automatic characterization and data collection from crystals of biological macromolecules. *Acta Crystallogr. Sect. D Biol. Crystallogr.* **71,** 1757–1767 CrossRef Medline

53. Kabsch, W. (2010) XDS. *Acta Crystallogr. D Biol. Crystallogr.* **66,** 125–132 CrossRef Medline

54. Keegan, R. M., and Winn, M. D. (2007) Automated search-model discovery and preparation for structure solution by molecular replacement. *Acta Crystallogr. D Biol. Crystallogr.* **63,** 447–457 CrossRef Medline

55. Winn, M. D., Ballard, C. C., Cowtan, K. D., Dodson, E. J., Emsley, P., Evans, P. R., Keegan, R. M., Krissinel, E. B., Leslie, A. G., McCoy, A., McNicholas, S. J., Murshudov, G. N., Pannu, N. S., Potterton, E. A., Powell, H. R., *et al.* (2011) Overview of the CCP4 suite and current developments. *Acta Crystallogr. D Biol. Crystallogr.* **67,** 235–242 CrossRef Medline

56. Joosten, R. P., Long, F., Murshudov, G. N., and Perrakis, A. (2014) The PDB_REDO server for macromolecular structure model optimization. *IUCrJ* **1,** 213–220 CrossRef Medline

57. Chen, V. B., Arendall, W. B., 3rd, Headd, J. J., Keedy, D. A., Immormino, R. M., Kapral, G. J., Murray, L. W., Richardson, J. S., and Richardson, D. C. (2010) MolProbity: all-atom structure validation for macromolecular crystallography. *Acta Crystallogr. D Biol. Crystallogr.* **66,** 12–21 CrossRef Medline

58. Krissinel, E., and Henrick, K. (2007) Inference of macromolecular assemblies from crystalline state. *J. Mol. Biol.* **372,** 774–797 CrossRef Medline

59. Battye, T. G. G., Kontogiannis, L., Johnson, O., Powell, H. R., and Leslie, A. G. W. (2011) iMOSFLM: a new graphical interface for diffraction-image processing with MOSFLM. *Acta Crystallogr. D Biol. Crystallogr.* **67,** 271–281 CrossRef Medline

60. Evans, P. (2006) Scaling and assessment of data quality. *Acta Crystallogr. D Biol. Crystallogr.* **62,** 72–82 CrossRef Medline

61. McCoy, A. J., Grosse-Kunstleve, R. W., Adams, P. D., Winn, M. D., Storoni, L. C., and Read, R. J. (2007) Phaser crystallographic software. *J. Appl. Crystallogr.* **40,** 658–674 CrossRef Medline

62. Kleywegt, G. J., Zou, J. Y., Kjeldgaard, M., Jones, T. A., (2001) Around O. In: *International Tables for Crystallography, Vol. F. Crystallography of Biological Macromolecules* (Rossmann, M. G., and Arnold, E., eds) pp. 353–367, Kluwer Academic Publishers, Dordrecht, The Netherlands

63. Mosca, R., and Schneider, T. R. (2008) RAPIDO: a web server for the alignment of protein structures in the presence of conformational changes. *Nucleic Acids Res.* **36,** W42–W46 CrossRef Medline

64. Franke, D., Petoukhov, M. V., Konarev, P. V., Panjkovich, A., Tuukkanen, A., Mertens, H. D. T., Kikhney, A. G., Hajizadeh, N. R., Franklin, J. M., Jeffries, C. M., and Svergun, D. I. (2017) ATSAS 2.8: a comprehensive data analysis suite for small-angle scattering from macromolecular solutions. *J. Appl. Crystallogr.* **50,** 1212–1225 CrossRef Medline

65. Rambo, R. P., and Tainer, J. A. (2013) Accurate assessment of mass, models and resolution by small-angle scattering. *Nature* **496,** 477–481 CrossRef Medline

66. Konarev, P. V., and Svergun, D. I. (2015) *A posteriori* determination of the useful data range for small-angle scattering experiments on dilute monodisperse systems. *IUCrJ* **2,** 352–360 CrossRef Medline

67. Petoukhov, M. V., and Svergun, D. I. (2015) Ambiguity assessment of small-angle scattering curves from monodisperse systems. *Acta Crystallogr. D Biol. Crystallogr.* **71,** 1051–1058 CrossRef Medline

68. Guinier, A. (1939) La diffraction des rayons X aux très petits angles: application à l'étude de phénomènes ultramicroscopiques. *Ann. Phys.* **11,** 161–237 CrossRef

69. Svergun, D. I. (1992) Determination of the regularization parameter in indirect-transform methods using perceptual criteria. *J. Appl. Crystallogr.* **25,** 495–503 CrossRef

70. Svergun, D., Barberato, C., and Koch, M. H. J. (1995) CRYSOL—a program to evaluate X-ray solution scattering of biological macromolecules from atomic coordinates. *J. Appl. Crystallogr.* **28,** 768–773 CrossRef

71. Panjkovich, A., and Svergun, D. I. (2016) Deciphering conformational transitions of proteins by small angle X-ray scattering and normal mode analysis. *Phys. Chem. Chem. Phys.* **18,** 5707–5719 CrossRef Medline